Journal of Sound and Vibration 333 (2014) 693–710

Contents lists available at ScienceDirect

Journal of Sound and Vibration

journal homepage: www.elsevier.com/locate/jsvi

Time domain responses of hydraulic bushing with two flow passages

Tan Chai, Jason T. Dreyer, Rajendra Singh *

Acoustics and Dynamics Laboratory, Smart Vehicle Concepts Center, Department of Mechanical Engineering, The Ohio State University, Columbus, OH 43210, USA

ARTICLE INFO

Article history:
Received 12 February 2013
Received in revised form
26 September 2013
Accepted 26 September 2013
Handling Editor: H. Ouyang
Available online 25 October 2013

ABSTRACT

Hydraulic bushings are commonly employed in vehicle suspension and body sub-frame systems to control motion, vibration, and structure-borne noise. Since literature on this topic is sparse, a controlled bushing prototype which accommodates a combination of long and short flow passages and flow restriction elements is first designed, constructed and instrumented. Step-up and step-down responses of several typical fluid-filled bushing configurations are measured along with steady harmonic time histories of transmitted force and internal pressures. To analyze the experimental results and gain physical insights into the hydraulic bushing system, lumped system models of bushings with different design features are developed, and analytical expressions of transmitted force and internal pressure responses are derived by using the convolution method. Parametric studies are also conducted to examine the effect of hydraulic element parameters. System parameters are successfully estimated for both harmonic and step responses using theory and measurements, and the dynamic force measurements are analyzed using analytical predictions. Finally, some nonlinearities of the system are also observed, and the fluid resistance of flow passage is found to be the most nonlinear element.

1. Introduction

1.1. Literature review

Hydraulic bushings are used as interfacial elements in vehicle suspensions and sub-frames for improved ride and handling performance while providing efficient structure-borne noise reduction and vibration isolation [1–3]. Unlike conventional rubber bushings, hydraulic devices yield higher damping and stiffness at lower frequencies, though they exhibit amplitude dependent properties [1–5]. The design features of hydraulic bushings are described in many patents [6–11]. For instance, Hipsher [6] invented a bushing composed of inner and outer metal sleeves and an elastomeric insert with two fluid chambers connected by a short tube. Konishi [7] proposed a device with a stopper fixed to the inner metal part to prevent excessive displacement and a fluid passageway that consists of holes and an annular groove. Kanda [8,9] designed several bushings that include a circumferential tube (known as the inertia track) and a combination of two parallel orifice passages with different areas. Roth and Henry [11] proposed various frequency-range specific inertia track and orifice type designs. Even though many patents [6–11] claim specific fluid-filled bushing performance features in the frequency

* Corresponding author. Tel.: +1 614 292 9044.
E-mail address: singh.3@osu.edu (R. Singh).

0022-460X/$ - see front matter © 2013 Elsevier Ltd. All rights reserved.
http://dx.doi.org/10.1016/j.jsv.2013.09.037

domain, no analytical justifications were provided. Further, very few scholarly articles have addressed the characterization and modeling issues of hydraulic bushings [12–16]. Limited articles on frequency domain models include work by Sauer and Guy [1], who briefly presented a numerical model for simulating a hydraulic bushing with an inertia track and a by-pass track (a controlled leakage path) in parallel, but no detailed description or simulation results were provided. Lu and Ari-Gur [12] derived a simple expression for the natural frequency of hydraulic bushings based on a linear model without presenting any experimental validation. Sevensson and Hakansson [14] proposed empirical models that included a nonlinear spring with a few coupled fluid elements, but such models are inaccurate, especially at the low excitation amplitudes. Arzanpour and Golnaraghi [15] described a linear model of the hydraulic engine sub-frame bushing, but their approach is virtually identical to the one for a hydraulic engine mount with a fixed decoupler [18]. Recently, Chai et al. [16] examined the typical frequency domain dynamic responses of hydraulic bushings.

Even though hydraulic bushing time domain properties play an important role in the investigation of the hydraulic damping effect on vehicle system performance, such as brake judder and shimmy [1], prior articles [1,12–16] have only examined the frequency domain properties, and most designs [1,6–11] are only based on spectral characteristics. Also, the precise relationship between hydraulic elements and dynamic responses has not been well established. Therefore, this article aims specifically to study the time domain characteristics of hydraulic bushings.

Although no literature is available on the time domain performance of hydraulic bushings, time domain responses of several hydraulic isolation and damping devices such as engine mounts [17–19] and shock absorbers [20] have been previously examined. For example, Yoon and Singh [18] estimated the force transmitted by a hydraulic mount in the time domain under sinusoidal excitation with a focus on the super-harmonic terms. Tiwari et al. [19] studied the steady state and transient responses of hydraulic engine mounts.

1.2. Scope and objectives

As shown in Fig. 1, a typical fluid-filled bushing usually consists of a rubber element interposed between the inner and outer metal sleeves and two similar fluid chambers connected by one or more flow passages [1,2]. The relative deflection of the inner and outer metal causes chamber pressures to vary, and thus the fluid (typically an anti-freeze and water mixture) flows back and forth through the passages to provide hydraulic damping. Note that although hydraulic bushings are conceptually similar to the hydraulic engine mount, their application, construction and dynamic properties are essentially different. In particular, a hydraulic mount (with a fixed or free decoupler) is widely used to support vehicle engines and control motion mostly at low frequencies. The excitation is applied to the top of the mount, its lower chamber is very compliant, and the pressure in the lower chamber is usually negligible compared with the upper chamber pressure. In contrast, a fluid-filled bushing does not include a decoupler mechanism, the two chambers are almost identical, the outer metal sleeve can be assumed to be fixed, and the excitation is applied to the inner metal part. Some bushing designs, however, have a leakage (by-pass) path in parallel with the inertia track to communicate fluid under high amplitude deflection [1]. Overall, the models developed for hydraulic engine mounts cannot be directly applied to fluid-filled bushings due to the differences discussed above.

Although hydraulic bushings exhibit frequency-dependent and amplitude-sensitive properties, a linear time invariant model must first be developed to understand the physical mechanism of the fluid-filled bushing system. Only radial damping is considered because the relative displacement between the inner and outer metal parts is assumed to be only in the radial direction. Accordingly, system parameters (based on the linear system theory) will first be estimated for sinusoidal cases by assuming low amplitude excitation and then for transient responses. Corresponding time domain experiments will include the measurements of transmitted (dynamic) force and internal fluid chamber pressures. The fluid

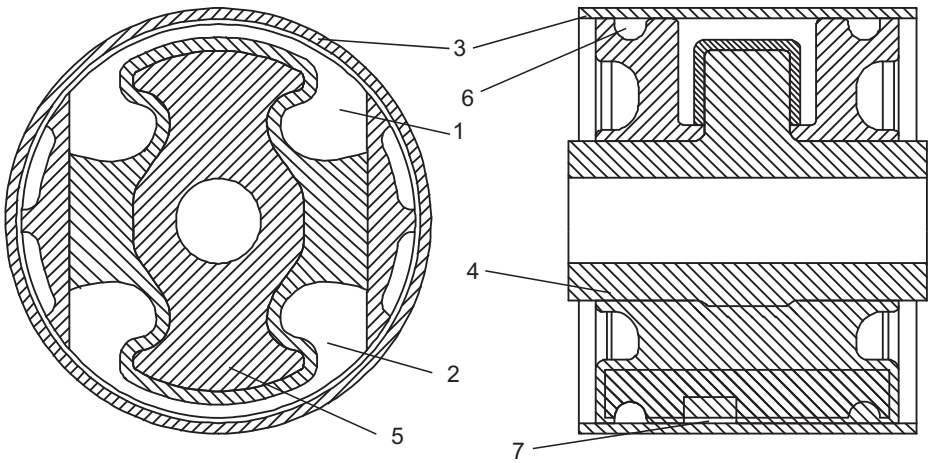

Fig. 1. Typical hydraulic bushing with inertia track and leakage path. Here 1 and 2 are the fluid chambers, 3 is the outer metal sleeve, 4 is the inner metal part, 5 is the stopper member, 6 is the inertia track, and 7 is the leakage path.

passages of production bushings have irregular geometry and are constructed with alternate materials from elastomers to metals [1–2,6–11]. Also, since the passages vary significantly from sample to sample, experimentation with many production bushings (from different manufacturers) would pose a very difficult task. Therefore, a laboratory device which can provide insights into salient features is needed for scientific examination. Accordingly, the specific objectives for this article are as follows: (1) design a laboratory bushing device with alternate configurations to conceptually examine commonly seen hydraulic passages and paths, and conduct time domain experiments with sinusoidal and step-up (or step-down) displacement excitations; (2) develop mathematical models of well-known configurations using only the linear system theory, and find closed form expressions for time domain responses; and (3) estimate system parameters for steady state and transient responses based on analytical expressions and experimental results, and analyze measured responses by utilizing the proposed models.

The organization of this article is as follows. First, the laboratory bushing device is discussed in Section 2. In order to examine typical fluid-filled bushing configurations, mathematical models and analytical expressions of steady state harmonic and transient responses are developed in Sections 3 and 4. The effect of key system parameters is examined in Section 5. Then the parameter estimation steps for sinusoidal and step responses are proposed in Section 6. Finally, measured time histories are analyzed in Sections 7 and 8 by utilizing the proposed linear models; sources of discrepancies between experiment and theory are explained as well.

2. Design of hydraulic bushing prototype for experimental studies

2.1. Conceptual fluid system model

A fluid system model of the bushing with two parallel passages is proposed in Fig. 2(a) based on a lumped parameter method. These include an internal long passage such as the inertia track (#*i*), though it is shown as an external tube in Fig. 2(a) for the sake of clarity, and/or a short passage (#*s*) with a flow restriction or controlled leakage element (such as the orifice). The long and short flow passages are represented by the fluid inertances I_i and I_s and fluid resistance R_i and R_s, respectively. The rubber element (#*r*) is modeled by rubber stiffness k_r and viscous damping coefficient c_r. The compliances of the two fluid chambers (#1 and #2) are C_1 and C_2, respectively, with effective pumping areas A_1 and A_2. Static ($\overline{x}$) and

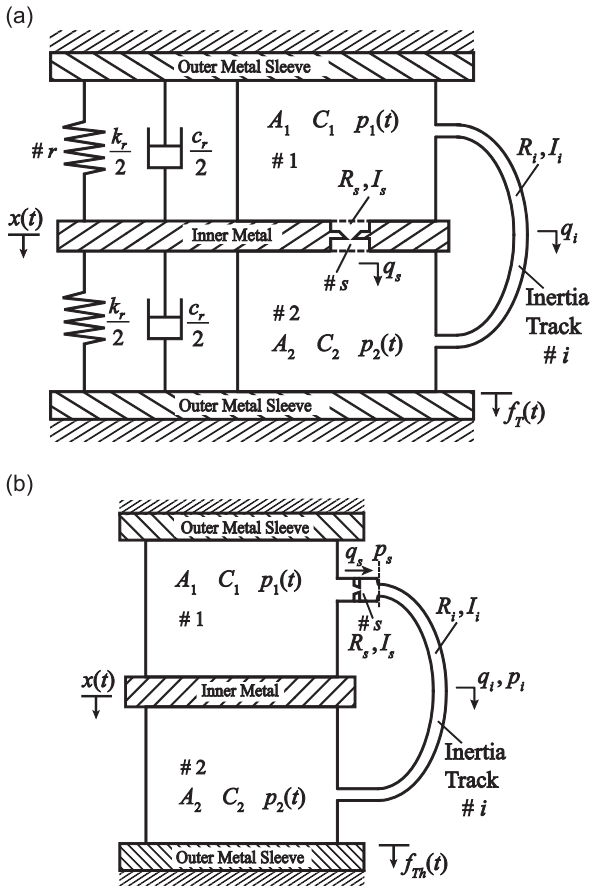

Fig. 2. Fluid system models of hydraulic bushing. (a) A conceptual model of bushing that consists of two compliance elements (denoted by #1 and 2), and two in-parallel fluid passages; (b) fluid path within series fluid passages. Key: #*i*: a long flow passage (say inertia track) and #*s*: a short flow passage with orifice-like restriction.

dynamic ($x(t)$) displacement excitations are applied to the inner metal part while the outer metal sleeve is fixed relative to the inner sleeve. The mean force f_m transmitted to the outer sleeve under a static displacement $\bar{x}$ is as follows, where $\bar{p}$ is the fluid chamber pressure under static equilibrium:

$$f_m = k_r\bar{x}+(A_2-A_1)\bar{p}. \tag{1}$$

The dynamic displacement excitation $x(t)$ from the static equilibrium is applied to the bushing under a mean load f_m. By applying a continuity equation to the fluid control volume elements, the following equations are obtained, where $q_i(t)$ and $q_s(t)$ are the volumetric flow rates through the long track and short passage, respectively and $p_1(t)$ and $p_2(t)$ are the dynamic pressures inside the two fluid chambers, respectively.

$$-A_1\dot{x}(t)-q_i(t)-q_s(t)=C_1\dot{p}_1(t),\quad A_2\dot{x}(t)+q_i(t)+q_s(t)=C_2\dot{p}_2(t), \tag{2a,b}$$

the application of the momentum equation to the flow passages yields the following:

$$p_1(t)-p_2(t)=I_i\dot{q}_i(t)+R_iq_i(t),\quad p_1(t)-p_2(t)=I_s\dot{q}_s(t)+R_sq_s(t). \tag{3a,b}$$

The dynamic force is transmitted to the outer sleeve by the rubber and hydraulic paths. Thus, the total transmitted force $f_T(t)$ is defined below, where $f_{\mathrm{Tr}}(t)$ is the rubber path force and $f_{\mathrm{Th}}(t)$ the hydraulic path force:

$$f_T(t)=f_{\mathrm{Tr}}(t)+f_{\mathrm{Th}}(t)+f_m. \tag{4}$$

2.2. Design of a hydraulic bushing prototype with multiple configurations

Since the internal parts of a production bushing are usually not available for experimental examination, the measurements of productive devices cannot provide an adequate understanding of the physical mechanism. Moreover, manufacturing many bushing samples for characterizing the fluid elements would be highly costly and difficult to accomplish in practice. Therefore, a laboratory prototype device which incorporates typical fluid-filled bushing design features is designed and constructed to simulate various production bushing dynamic behaviors and gain insights into the time domain properties. Since most bushing designs include one or more flow passages connecting two hydraulic chambers [1,2,6–11], the laboratory device with multiple configurations has been designed and fabricated so as to vary the fluid paths in a controlled manner. This prototype, as shown in Fig. 3, consists of two fluid chambers, a customized mid-plate, two external long fluid passages, two short fluid passages with restrictions, and fixtures. Since the two hydraulic chambers in production bushings usually are similar, the fluid chambers of this device are formed by using two almost identical mount parts, which consist of rubber elements and steel brackets. The volume of each chamber is around 54 ml. The hardness of the natural rubber material is 60 durometer (Shore A), and the static stiffness of the drained prototype is around 500 N/mm. The mid-plate is designed to connect two chambers in various ways and to accommodate pressure sensors. The fluid passages, which are located in the mid-plate as shown in Figs. 3 and 4(a), are routed externally for the sake of fabrication and easy connection or disconnection. One long fluid passage is facilitated via one external metal tube of internal diameter d_i=4.72 mm and length l_i=447.65 mm and a ball valve at the inlet (or outlet) which controls the opening or closing of this particular flow passage. The short fluid passage with a diameter of 6.83 mm and a length of 61.93 mm is formed by utilizing a needle valve that is placed in the mid-plate. A color coded handle thread of this valve provides a reference for setting repeated flow conditions. By adjusting the cross-sectional area of the passage via the needle valve, this device is able to provide a combination of a parallel long track and a short fluid passage with an adjustable flow restriction, as well as the single flow passage configuration. Moreover, another needle valve is placed at the end of a second long passage, which can then simulate two passages in series. Finally, two dynamic pressure transducers (PCB Model #102A05) are installed in the mid-plate and connected to two fluid chambers to measure internal dynamic pressures.

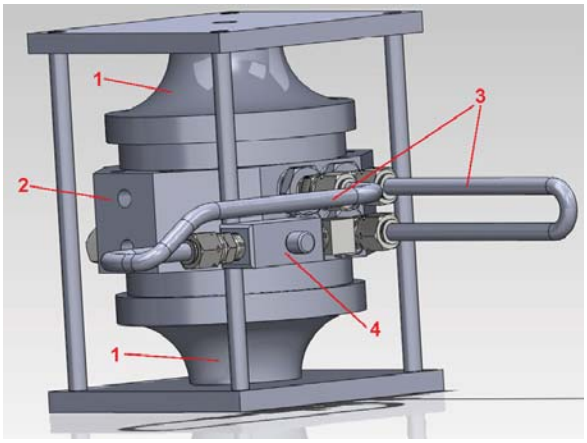

Fig. 3. Design of laboratory prototype bushing. Here 1 is the fluid chamber, 2 is the mid-plate, 3 is the long fluid passage, and 4 is the short fluid passage with flow restriction. Another short passage and two pressure sensors are embedded in the back side of the mid-plate (not shown in this figure).

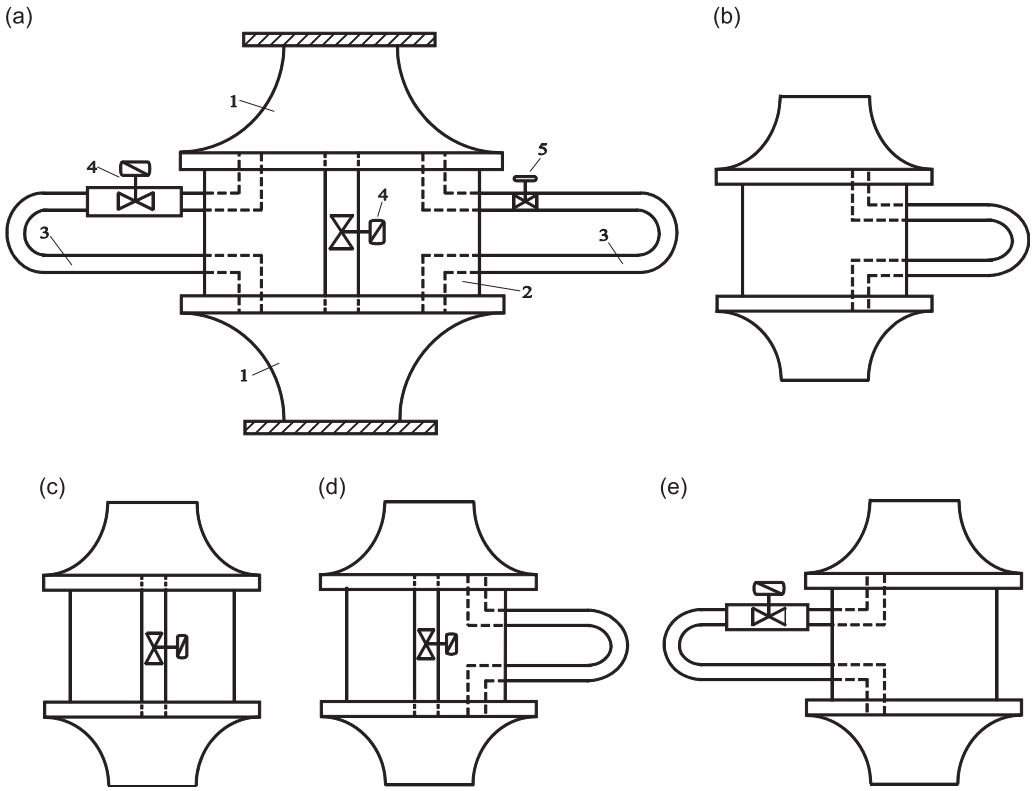

Fig. 4. Multiple configurations of the hydraulic bushing prototype constructed for controlled laboratory studies. (a) Schematic of the prototype with external fluid passages. Here 1 is the fluid chamber, 2 is the mid-plate, 3 is a long fluid passage, 4 is a short fluid passage with restriction, and 5 is a flow control valve; (b) configuration B1 with long fluid passage of diameter d_i; (c) configuration B2 with short flow passage with restriction of diameter $d_o=2d_i/3$ and configuration B3 $d_o=2d_i/9$; (d) configuration B4 with parallel long and short flow passages with $d_o=2d_i/3$ and B5 with $d_o=2d_i/9$; (e) configurations B6 and B7 with long and short flow passages in series (with $d_o=2d_i/3$ for B6 and with $d_o=2d_i/9$ for B7). Refer to Table 1 for a listing as well.

Table 1
Hydraulic bushing configurations developed for experimental studies.

Configuration of Fig. 4	Description
B1	One long passage of diameter d_i
B2	One short passage with a restriction of diameter $d_o \approx 2d_i/3$
B3	One short passage with a restriction of diameter $d_o \approx 2d_i/9$
B4	One long passage and one short passage with $d_o \approx 2d_i/3$ in parallel
B5	One long passage and one short passage with $d_o \approx 2d_i/9$ in parallel
B6	One long passage and one short passage with $d_o \approx 2d_i/3$ in series
B7	One long passage and one short passage with $d_o \approx 2d_i/9$ in series
B0	All fluid passages closed

To study commonly seen fluid-filled bushing designs, seven configurations of the prototype, as listed in Table 1 and illustrated in Fig. 4(b) to (e), are examined. The first configuration (designated B1) is evaluated when both needle valves are closed and the two hydraulic chambers are connected by only one long passage. This configuration simulates the most common practical device with only an inertia track [1,2,8,10–15]. Second, B2 and B3 configurations, with the short passages only, are investigated; configuration B3 simulates an abrupt reduction in the flow area via a needle valve (diameter $d_o=2d_i/3$), while B2 employs a less restricted area (diameter $d_o=2d_i/9$). Third, an in-parallel combination of long and short passages is examined first with the B4 configuration with $d_o=2d_i/3$ and then with B5 with $d_o=2d_i/9$. These two configurations attempt to simulate in parallel designs [1,9]. Finally, some production devices have restricted orifices at the inlet or/and outlet of the inertia track, which could provide more flexibility in practical fluid passages designs. To examine such devices, the long and short passages are placed in series to form B6 (with $d_o=2d_i/3$) and B7 (with $d_o=2d_i/9$) configurations.

2.3. Experimental studies

Since the energy losses at the sharp-edged entrance/exit, pipe fitting, bending and irregular shape of the tube, etc., cannot be neglected, bench experiments are conducted on the mid-plate to measure the steady flow rate q and pressure drop Δp for each (isolated) passage. The inlet of one fluid passage is connected to a transparent vertical tube containing

liquid from a flow source while the outlet is open to the air. By adjusting the flow rate of the fluid source, a steady liquid level h is maintained, and then Δp is determined from ρgh, where ρ is the density of the liquid, and g is the gravitational acceleration. Meanwhile, the steady flow rate q is estimated from the accumulated fluid volume from the outlet over a known time duration. Then the characteristics of each flow passage are determined by examining the relationship between q and Δp. These experiments are, however, limited to lower pressure ranges.

Dynamic experiments on the above mentioned configurations are conducted using a non-resonant elastomer test machine (MTS 831.50, [21]). In addition, a limiting case B0, when all the fluid passages are closed, is also evaluated. In the steady-state experiment, a sinusoidal displacement excitation $x(t)=A\sin\omega t$ is applied to the device under a mean load, where A is the amplitude of harmonic input, $\omega=2\pi f$ is the excitation frequency in radians, and f is in Hz. The transmitted force $f_T(t)$ and dynamic pressure inside two chambers, $p_1(t)$ and $p_2(t)$, are measured from 1 to 60 Hz in 1 Hz increments at two amplitudes, $X=0.1$ and 1.0 mm, where $X=2A$ is the peak to peak (p–p) value. The dynamic stiffness ($K_d(\omega)$) measurements of selected configurations are shown in Fig. 5 given excitation amplitude $X=0.1$ and 1.0 mm. Here, the stiffness magnitude ($|K_d|$) is presented in a dimensionless form ($\overline{|K_d|}$), which is normalized by the static stiffness (k_{static}) of the prototype. For an easier comparison, the frequency scale is normalized by the frequency corresponding to the maximum loss angle (ϕ_K) of the B1 configuration. Observe that the responses can be grouped into three broad categories. The configurations dominated by the long inertia track, such as B1, B5, and B6, exhibit high peak stiffness and loss angles at a lower frequency (about 10 Hz), while the $K_d(\omega)$ of B2 and B4 show lower peak $|K_d|$ and ϕ_K at higher frequencies (frequency of maximum is about 25 Hz); these are dominated by a short and somewhat restricted passage. Finally, B3 and B7 have relatively lower $|K_d|$ and ϕ_K values since only a limited amount of fluid is communicated between two chambers due to significant restriction inside the short passage. Moreover, when X is increased from 0.1 to 1.0 mm, both $|K_d|$ and ϕ_K decrease, especially for the long inertia track configuration. The frequencies corresponding to peak magnitude and peak loss angle decrease as well.

In the transient experiment, a step-up or step-down excitation is applied to the prototype, and only the transmitted force is measured. The internal pressure signals, $p_{1,2}(t)$, are not available in this experiment because the sampling frequency exceeds the range of the auxiliary channel in the test machine. As shown in Fig. 6(a), first a compressive mean load $f_m=500$ N corresponding to displacement $x_M(t)=A_0$ is applied; next, the step-up process increases the load to reach $x_M(t)=A_0+A_x$ and holds it for $\Delta t=t_2-t_1$; then $x_M(t)$ is released to A_0-A_x via the step-down process and is held for another $\Delta t=t_3-t_2$. Finally, the load is increased back to around 500 N such that now $x_M(t)\approx A_0$. The ideal input signal of Fig. 6(a) can be expressed in terms of the unit step (Heaviside) function $u(t)$ as:

$$x_M(t)=A_0+A_x u(t-t_1)-2A_x u(t-t_2)+A_x u(t-t_3), \tag{5}$$

however, an ideal step function is extremely difficult to generate given the practical limitations of the actuator. Thus, only step-like functions such as smoothened step-up or step-down events are realized as shown in Fig. 6(b). Note that the step-down excitation has twice the height A_e of the step-up, and their initial loading levels are different. Thus, this measurement

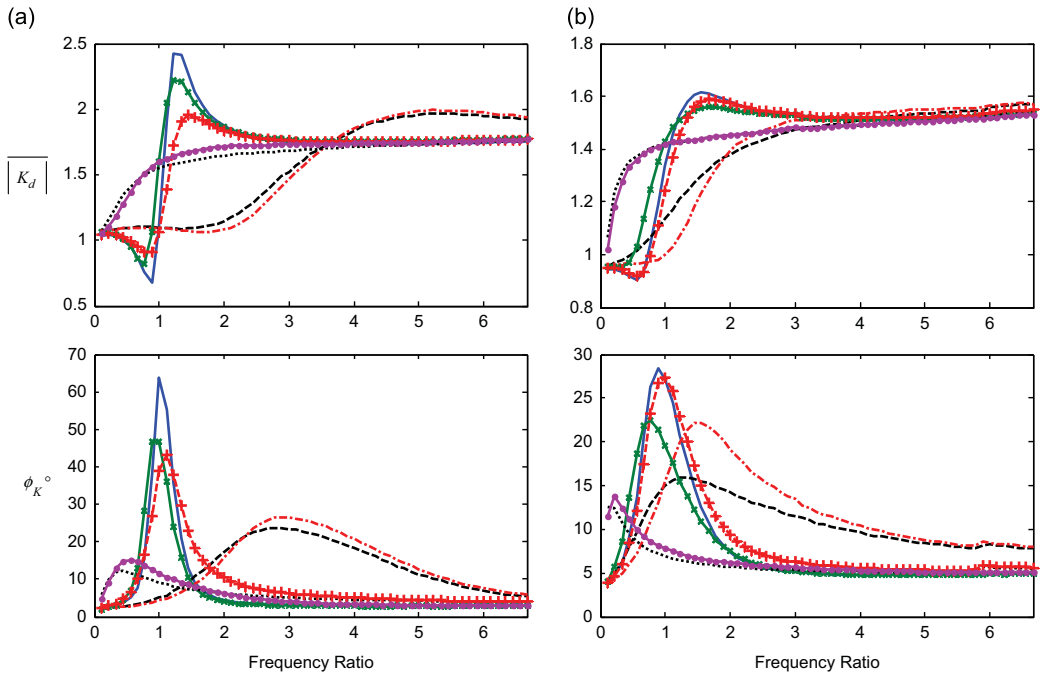

Fig. 5. Dynamic stiffness spectra of seven configurations of the prototype bushing of Fig. 4 and Table 1. (a) $X=0.1$ mm; (b) $X=1.0$ mm. Key: ——, B1; – – –, B2; ……, B3; – · – · –, B4; – + –, B5; –×–, B6; –●–, B7.

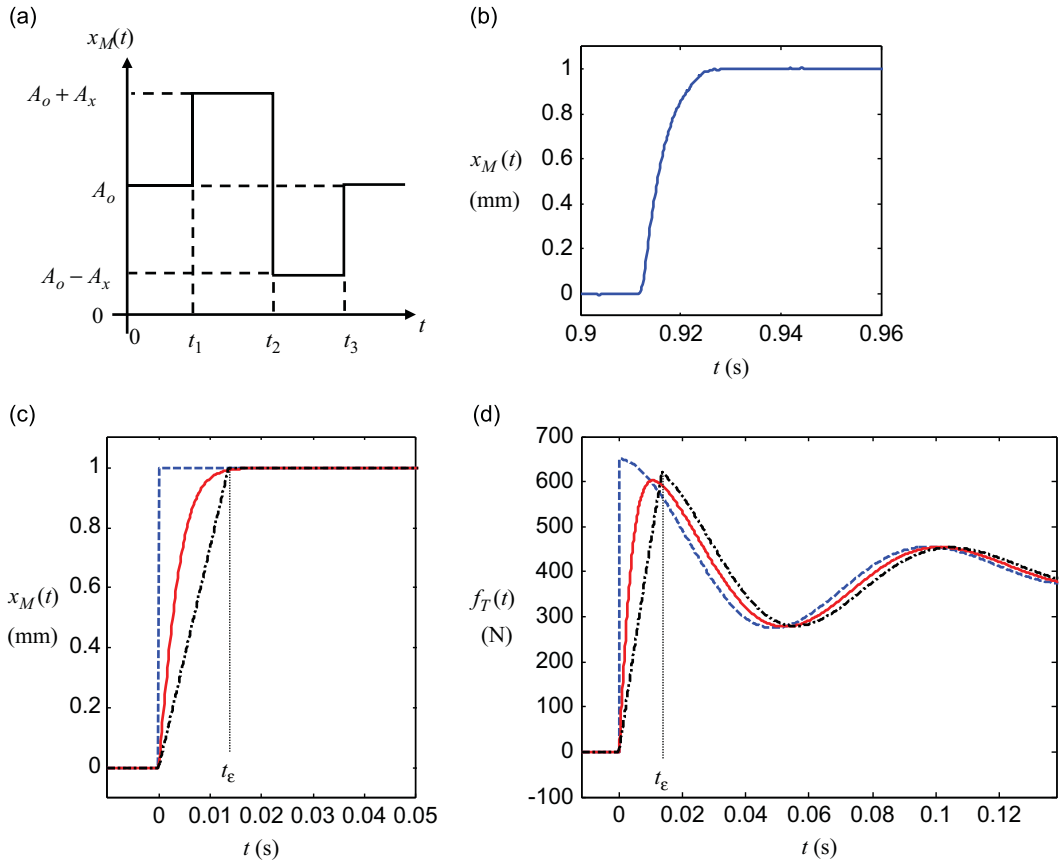

Fig. 6. Displacement excitation profiles for the transient experiment. (a) Ideal step-up and step-down pulse; (b) smoothened step-up excitation as measured in the experiment; (c) comparison of three analytical approximations of the step excitation; (d) step responses corresponding to three displacement profiles. Key: – – –, ideal step input; ——, approximated smoothened step input using hyperbolic function; – · – · –, approximated by ramp function.

will investigate the effect of A_e and the mean load on transient responses. The experimental results will be discussed in detail along with analytical predictions in Sections 7 and 8.

3. Analytical models for several configurations

3.1. Model I for long and short flow passages in parallel

An analogous mechanical system model of Fig. 2(a) is developed where the hydraulic path includes long (inertia track) and short passages in parallel. The reason for selecting this model is that it should facilitate an easier implementation into vehicle structural models. The rubber path is still approximated by the Kelvin–Voigt model with rubber stiffness k_r and damping coefficient c_r. The effective fluid path parameters based on the fluid system model discussed in Section 2.1 are defined as follows: equivalent mechanical stiffness of two fluid chamber compliances $k_1 = A_1^2/C_1$ and $k_2 = A_2^2/C_2$, effective cross-sectional area of the inertia track $A_{ie} = \sqrt{(A_1^2C_2 + A_2^2C_1)/(C_1 + C_2)}$, effective fluid velocity in the inertia track $\dot{x}_{ie}(t) = q_i(t)/A_{ie}$, effective mass of the inertia track fluid $m_{ie} = A_{ie}^2 I_i$, effective viscous damping of inertia track fluid $c_{ie} = A_{ie}^2 R_i$, effective cross-sectional area of the short flow passage $A_{se} = \sqrt{(A_1^2C_2 + A_2^2C_1)/(C_1 + C_2)}$, effective fluid velocity in the short track $\dot{x}_{se}(t) = q_s(t)/A_{se}$, effective mass of the short passage fluid $m_{se} = A_{se}^2 I_s$, and effective viscous damping of the short passage fluid $c_{se} = A_{se}^2 R_s$. Assuming the bushing mass (m_r) to be negligible, the transmitted (dynamic) force is given as

$$f_T(t) = f_{Tr}(t) + f_{Th}(t) = [k_r x(t) + c_r \dot{x}(t)] + (k_1 + k_2)[x(t) + x_{ie}(t) + x_{se}(t)], \tag{6}$$

application of Newton's second law to the inertia track and short passage fluid elements yields the following governing equations:

$$m_{ie}\ddot{x}_{ie}(t) + c_{ie}\dot{x}_{ie}(t) + (k_1 + k_2)x_{ie}(t) = -(k_1 + k_2)[x(t) + x_{se}(t)], \tag{7a}$$

$$m_{se}\ddot{x}_{se}(t) + c_{se}\dot{x}_{se}(t) + (k_1 + k_2)x_{se}(t) = -(k_1 + k_2)[x(t) + x_{ie}(t)], \tag{7b}$$

by transforming Eq. (6) to (7) into the Laplace domain and assuming zero initial conditions, the dynamic stiffness K_d is obtained as follows, where the hydraulic path given by $K_{dh}(s)=F_{Th}/X(s)$ is a 3rd/3rd-order system:

$$K_d(s)=\frac{F_T}{X}(s)=\frac{F_{Tr}}{X}(s)+\frac{F_{Th}}{X}(s),\quad \frac{F_{Tr}}{X}(s)=k_r+c_rs, \tag{8a,b}$$

$$\frac{F_{Th}}{X}(s)=\frac{(k_1+k_2)s(m_{ie}s+c_{ie})(m_{se}s+c_{se})}{m_{ie}m_{se}s^3+(m_{se}c_{ie}+m_{ie}c_{se})s^2+[(k_1+k_2)(m_{ie}+m_{se})+c_{ie}c_{se}]s+(k_1+k_2)(c_{ie}+c_{se})}. \tag{8c}$$

Next, assume that the short passage acts like a sharp-edged orifice when the cross-sectional area of its restriction is much smaller than that of the flow passage, as designed in configuration B5. Also assume that this orifice-like element (including surrounding entrance and exit losses and momentum) is derived by resistance R_o and inertance I_o elements. Effective velocity in the orifice (given volume flow rate q_o) is defined as $\dot{x}_{oe}(t)=q_o(t)/A_{oe}$, where the effective orifice mass is $m_{oe}=A_{oe}^2I_o$, effective viscous damping is $c_{oe}=A_{oe}^2R_o$, and $A_{oe}=\sqrt{(A_1^2C_2+A_2^2C_1)/(C_1+C_2)}$ is the effective cross-sectional area of the orifice. Thus, for a bushing with assumed inertia track and orifice-like elements in parallel, m_{se} and c_{se} in Eq. (8) are replaced by m_{oe} and c_{oe}, respectively. Since m_{oe} is usually negligible at the lower frequencies, Eq. (8) is simplified to a reduced order form as follows:

$$K_d(s)=k_r+c_rs+(k_1+k_2)\frac{c_{oe}s(m_{ie}s+c_{ie})}{m_{ie}c_{oe}s^2+[m_{ie}(k_1+k_2)+c_{ie}c_{oe}]s+(k_1+k_2)(c_{ie}+c_{oe})}, \tag{9}$$

note that K_{dh} is reduced to a 2nd/2nd-order system. Further, convert Eq. (9) into a standard form as follows, where γ is the combined static stiffness of two fluid chambers, τ is the time constant in the numerator, and ω_{n2} and ζ_2 are the natural frequency and damping ratio of the denominator expression, respectively.

$$K_d(s)=k_r+c_rs+\gamma\frac{s(s+\tau)}{s^2+2\zeta_2\omega_{n2}s+\omega_{n2}^2}, \tag{10a}$$

$$\gamma=k_1+k_2,\quad \tau=\frac{c_{ie}}{m_{ie}},\quad \omega_{n2}=\sqrt{\frac{(k_1+k_2)(c_{ie}+c_{oe})}{m_{ie}c_{oe}}},\quad \zeta_2=\frac{(k_1+k_2)m_{ie}+c_{ie}c_{oe}}{2\sqrt{(k_1+k_2)(c_{ie}+c_{oe})m_{ie}c_{oe}}}. \tag{10b–e}$$

3.2. Model II for a single fluid passage

A hydraulic bushing design with only one long flow passage, such as in the B1 configuration, can be analyzed as a sub-set of the mechanical system in Section 3.1. The following governing equations are found by assuming that $x_{se}=0$, $m_{se}=0$ and $c_{se}\to\infty$:

$$f_T(t)=k_rx(t)+c_r\dot{x}(t)+(k_1+k_2)[x(t)+x_{ie}(t)], \tag{11}$$

$$m_{ie}\ddot{x}_{ie}(t)+c_{ie}\dot{x}_{ie}(t)+(k_1+k_2)x_{ie}(t)=-(k_1+k_2)x(t), \tag{12}$$

the dynamic stiffness of a bushing with one inertia track is obtained by transforming Eqs. (11) and (12) into the Laplace domain:

$$K_d(s)=k_r+c_rs+(k_1+k_2)\frac{m_{ie}s^2+c_{ie}s}{m_{ie}s^2+c_{ie}s+k_1+k_2}, \tag{13}$$

also, Eq. (13) is converted into a standard form as follows where $\gamma=k_1+k_2$ and $\tau=c_{ie}/m_{ie}$ are the same as in Eq. (10):

$$K_d(s)=k_r+c_rs+\gamma\frac{s(s+\tau)}{s^2+2\zeta_2\omega_{n2}s+\omega_{n2}^2}, \tag{14a}$$

$$\omega_{n2}=\sqrt{(k_1+k_2)/m_{ie}},\quad \zeta_2=\tfrac{1}{2}\sqrt{c_{ie}^2/[m_{ie}(k_1+k_2)]}, \tag{14b,c}$$

similarly, the dynamic stiffness of a bushing with one short flow restriction (such as B2) is obtained by replacing m_{ie} and c_{ie} in Eq. (13) by the effective mass m_{se} and damping c_{se}. Key parameters for models I and II (from Eqs. (10) and (14)) are summarized in Table 2.

3.3. Model III for long and short passages in series

The fluid model for a bushing with in-series long and short passages is developed in Fig. 2(b). The compliance of the long passage C_i was neglected in models I and II since its value is three magnitudes smaller than the C_1 and C_2 elements. However, C_i must be included in model III to calculate the difference between q_i and q_s. By applying the continuity and

Table 2
System parameters of analytical models based on the linear system theory.

Standard system parameters	Model I	Model II		
		Used for B1	Used for B2	Used for B3
γ	k_1+k_2	k_1+k_2	k_1+k_2	k_1+k_2
τ	c_{ie}/m_{ie}	c_{ie}/m_{ie}	c_{se}/m_{se}	–
ω_{n2}	$\sqrt{\frac{(k_1+k_2)(c_{ie}+c_{oe})}{m_{ie}c_{oe}}}$	$\sqrt{\frac{k_1+k_2}{m_{ie}}}$	$\sqrt{\frac{k_1+k_2}{m_{se}}}$	–
ζ_2	$\frac{(k_1+k_2)m_{ie}+c_{ie}c_{oe}}{2\sqrt{(k_1+k_2)(c_{ie}+c_{oe})m_{ie}c_{oe}}}$	$\frac{c_{ie}}{2\sqrt{m_{ie}(k_1+k_2)}}$	$\frac{c_{se}}{2\sqrt{m_{se}(k_1+k_2)}}$	–
τ_2	–	–	–	$(k_1+k_2)/c_{oe}$

momentum equations to the fluid path, the following equations are obtained:

$$-A_1\dot{x}(t)-q_s(t)=C_1\dot{p}_1(t),\quad A_2\dot{x}(t)+q_i(t)=C_2\dot{p}_2(t),\quad q_s(t)-q_i(t)=C_i\dot{p}_i(t), \tag{15a–c}$$

$$p_1(t)-p_s(t)=I_s\dot{q}_s(t)+R_sq_s(t),\quad p_s(t)-p_2(t)=I_i\dot{q}_i(t)+R_iq_i(t)+\frac{1}{C_i}\int q_i(t)dt, \tag{15d,e}$$

where $p_s(t)$ is the dynamic pressure at the end of the short fluid passage, and $p_i(t)=0.5[p_s(t)+p_2(t)]/2$ is the mean pressure inside the long passage.

An analogous mechanical model for a bushing with the long and short flow passages in series (such as B6) is developed as well. Note that the effective stiffness of the inertia track, $k_{ie}=A_{ie}^2/C_i$, is much higher than k_1 and k_2. Other effective hydraulic path parameters are the same as defined in Section 3.1. The following equations of motion are obtained for the hydraulic path:

$$m_{se}\ddot{x}_{se}(t)+c_{se}\dot{x}_{se}(t)+(k_1+k_{ie})x_{se}(t)=k_{ie}x_{ie}(t)-k_1x(t), \tag{16a}$$

$$m_{ie}\ddot{x}_{ie}(t)+c_{ie}\dot{x}_{ie}(t)+(k_2+k_{ie})x_{ie}(t)=k_{ie}x_{se}(t)-k_2x(t), \tag{16b}$$

the transmitted (dynamic) force is given as

$$f_T(t)=k_rx(t)+c_r\dot{x}(t)+k_1[x(t)+x_{se}(t)]+k_2[x(t)+x_{ie}(t)], \tag{17}$$

by defining the dynamic stiffness of the long and short fluid passages as $K_i=m_{ie}s^2+c_{ie}s+k_2+k_{ie}$ and $K_s=m_{se}s^2+c_{se}s+k_1+k_{ie}$, respectively, the following motion transmissibility type transfer functions are obtained:

$$\frac{X_{ie}}{X}=\frac{k_{ie}k_1+k_2K_s}{k_{ie}^2-K_iK_s},\quad \frac{X_{se}}{X}=\frac{k_{ie}k_2+k_1K_i}{k_{ie}^2-K_iK_s}, \tag{18a,b}$$

finally, the dynamic stiffness is given as follows:

$$K_d(s)=\frac{F_T}{X}(s)=k_r+c_rs++k_1+k_2+\frac{K_ik_1^2+K_sk_2^2+2k_1k_2k_{ie}}{k_{ie}^2-K_iK_s}, \tag{19}$$

similarly, if the orifice element's dynamic stiffness is defined as $K_o=m_{oe}s^2+c_{oe}s+k_1+k_{oe}$, the overall dynamic stiffness of a bushing with a long fluid passage and an orifice-like element, such as B7, is obtained by replacing K_s by K_o in Eq. (19).

4. Closed form expressions of time domain responses using analytical models

4.1. Steady state harmonic response in time domain

Analytical expressions of $f_T(t)$, $p_1(t)$, and $p_2(t)$ under sinusoidal excitation are derived first. As discussed in Section 3, the dynamic stiffness of hydraulic path $K_{dh}(s)$ in model I or II can be written as

$$K_{dh}(s)=\gamma\frac{s(s+\tau)}{s^2+2\zeta_2\omega_{n2}s+\omega_{n2}^2}, \tag{20}$$

convert the above in the following form for model I of a bushing with a long flow passage and an orifice-like element in parallel, with parameters γ, τ, ω_{n2}, and ζ_2 as listed in Table 2:

$$K_{dh}(s)=\gamma\left[1-\frac{\omega_{n2}^2}{s^2+2\zeta_2\omega_{n2}s+\omega_{n2}^2}-\frac{(2\zeta_2\omega_{n2}-\tau)s}{s^2+2\zeta_2\omega_{n2}s+\omega_{n2}^2}\right], \tag{21}$$

when the sinusoidal displacement input $x(t)=A\sin\omega t$ is applied, the steady harmonic force transmitted by the rubber path is

$$f_{Tr}(t)=k_rx(t)+c_r\dot{x}(t)=k_rA\ \sin\ \omega t+c_rA\omega\ \cos\ \omega t, \tag{22}$$

the force transmitted by the hydraulic path is derived by the convolution ($\otimes$) of $x(t)$ and $h_{dh}(t)$, where $h_{dh}(t)=L^{-1}\{K_{dh}(s)\}$ is the impulse response corresponding to K_{dh}:

$$f_{Th}(t)=h_{dh}(t)\otimes x(t)=\int_0^t h_{dh}(\tau)x(t-\tau)d\tau, \tag{23}$$

$$h_{dh}(t)=\gamma\left[\delta(t)-\frac{\omega_{n2}}{\sqrt{1-\zeta_2^2}}e^{-\zeta_2\omega_{n2}t}\ \sin(\omega_d t)+\frac{2\zeta_2\omega_{n2}-\tau}{\sqrt{1-\zeta_2^2}}e^{-\zeta_2\omega_{n2}t}\ \sin(\omega_d t-\phi)\right], \tag{24}$$

where $\omega_d=\omega_{n2}\sqrt{1-\zeta_2^2}$, and $\phi=\tan^{-1}(\sqrt{1-\zeta_2^2}/\zeta_2)$. Then substitute Eq. (24) into Eq. (23) and integrate from 0 to t to find $f_{Th}(t)$ as:

$$f_{Th}(t)=A\gamma\ \sin\ \omega t-A\gamma\frac{\omega_{n2}}{2\sqrt{1-\zeta_2^2}}\left\{\frac{1}{\Gamma_1}E_1(t)+\frac{1}{\Gamma_2}E_2(t)\right\}+A\gamma\frac{(2\zeta_2\omega_{n2}-\tau)}{2\sqrt{1-\zeta_2^2}}\left\{\frac{1}{\Gamma_1}E_3(t)+\frac{1}{\Gamma_2}E_4(t)\right\}, \tag{25a}$$

$$E_1(t)=e^{-at}b\ \sin\ \omega_d t-e^{-at}a\ \cos\ \omega_d t+b\ \sin\ \omega t+a\ \cos\ \omega t, \tag{25b}$$

$$E_2(t)=e^{-at}c\ \sin\ \omega_d t+e^{-at}a\ \cos\ \omega_d t-c\ \sin\ \omega t-a\ \cos\ \omega t, \tag{25c}$$

$$E_3(t)=e^{-at}b\ \sin(\omega_d t-\phi)-e^{-at}a\ \cos(\omega_d t-\phi)+b\ \sin(\omega t-\phi)+a\ \cos(\omega t-\phi), \tag{25d}$$

$$E_4(t)=e^{-at}c\ \sin(\omega_d t-\phi)+e^{-at}a\ \cos(\omega_d t-\phi)-c\ \sin(\omega t-\phi)-a\ \cos(\omega t-\phi), \tag{25e}$$

$$\Gamma_1=\omega^2+\omega_{n2}^2+2\omega_d\omega,\quad \Gamma_2=\omega^2+\omega_{n2}^2-2\omega_d\omega, \tag{25f,g}$$

$$a=\omega_{n2}\zeta_2,\quad b=\omega+\omega_d,\quad c=\omega-\omega_d. \tag{25h,j}$$

For model II of a bushing with only a long flow passage (as in B1), the K_{dh} and f_{Th} expressions are simplified by setting $2\zeta_2\omega_{n2}=\tau$ in Eqs. (21) and (25), where parameters γ, ω_{n2}, ζ_1 and ζ_2 are listed in Table 2. Finally, the total transmitted force $f_T(t)=f_{Tr}(t)+f_{Th}(t)+f_m$ is estimated by using Eqs. (22) and (25) under a given mean load.

4.2. Transient response to an ideal step excitation

For an ideal step displacement input $x(t)=A_x u(t)$, the dynamic force transmitted by the rubber path $f_{Tr}(t)$ is

$$f_{Tr}(t)=k_r x(t)+c_r\dot{x}(t)=k_r A_x u(t)+c_r A_x\delta(t), \tag{26}$$

for a bushing with long and short flow passages in parallel, the force transmitted by the hydraulic path is obtained by the convolution method as

$$f_{Th}(t)=h_{dh}(t)\otimes x(t)=\frac{\gamma A_x}{\omega_d}e^{-at}(a\ \sin\ \omega_d t+\omega_d\ \cos\ \omega_d t)$$
$$-\gamma A_x\frac{2\zeta_2\omega_{n2}-\tau}{\omega_d\omega_{n2}}\{e^{-at}[a\ \sin(\omega_d t-\phi)+\omega_d\ \cos(\omega_d t-\phi)]+a\ \sin\ \phi-\omega_d\ \cos\ \phi\}, \tag{27}$$

where $h_{dh}(t)$, ω_d, a, ω_{n2}, and ζ_2 are derived as in Eqs. (22)–(25). For a bushing with only a long passage, the above step response is simplified since $2\zeta_2\omega_{n2}-\tau=0$. Note that for either model I or II, $f_{Th}(t)\to 0$ when $t\to\infty$.

4.3. Transient responses to smoothened step-up and step-down displacement excitations

4.3.1. Excitation approximated by hyperbolic–tangent function

The smoothened step-up excitation as implemented in the experiment and shown in Fig. 6(b) is analytically approximated by a hyperbolic–tangent function as follows where σ is a regularizing factor:

$$x(t)\approx A_x\ \tanh(\sigma t), \tag{28}$$

assuming the Kelvin–Voigt model for the rubber path, $f_{Tr}(t)$ to the smoothened step excitation is

$$f_{Tr}(t)=A_x[k_r\ \tanh(\sigma t)+c_r\sigma\,\mathrm{sech}^2(\sigma t)], \tag{29}$$

the force transmitted by the hydraulic path $f_{Th}(t)$ of a bushing with long track and orifice-like element in parallel (as in B5) is obtained using the convolution method as follows:

$$f_{Th}(t)=h_{dh}(t)\otimes x(t)=\gamma A_x\ \tanh(\sigma t)-\gamma A_x+\frac{\gamma A_x}{\omega_d}\{e^{-at}[a\ \sin\ \omega_d t+\omega_d\ \cos\ \omega_d t]+2\omega_{n2}^2\Delta_1(t)\}$$
$$-\gamma A_x\frac{2\zeta_2\omega_{n2}-\tau}{\omega_d\omega_{n2}}\{e^{-at}[a\ \sin(\omega_d t-\phi)+\omega_d\ \cos(\omega_d t-\phi)]+a\ \sin\ \phi-\omega_d\ \cos\ \phi+2\omega_{n2}^2\Delta_2(t)\}, \tag{30}$$

where $\Delta_1(t)$ and $\Delta_2(t)$ are expressions of two hyper geometric functions. Then, the total transmitted force is obtained by $f_T(t)=f_{\mathrm{Tr}}(t)+f_{\mathrm{Th}}(t)+f_m$.

4.3.2. Excitation approximated by ramp function

The ramp function may also be utilized to analytically approximate the non-ideal step excitation implemented in the experiment. Assuming that the excitation starts at $t=0$ and takes time t_ε to reach a step height A_x under a constant rate, the non-ideal step input is approximated as follows:

$$x(t)\approx \frac{A_x}{t_\varepsilon}tu(t)-\frac{A_x}{t_\varepsilon}(t-t_\varepsilon)u(t-t_\varepsilon), \tag{31}$$

thus, the force transmitted via the rubber path is

$$f_{\mathrm{Tr}}(t)=\frac{k_rA_x}{t_\varepsilon}[tu(t)-(t-t_\varepsilon)u(t-t_\varepsilon)]+\frac{c_rA_x}{t_\varepsilon}[u(t)-u(t-t_\varepsilon)]. \tag{32}$$

For a bushing with long and short passages in parallel, the force transmitted by the hydraulic path is obtained by the convolution method, using the system parameters of Table 2 corresponding to model I:

$$f_{\mathrm{Th}}(t)=\int_0^t h_{\mathrm{dh}}(\tau)x(t-\tau)d\tau=\frac{\gamma A_x}{t_\varepsilon\omega_d\omega_{n2}^2}[H_1(t)-H_1(t-t_\varepsilon)]-\frac{\gamma A_x(2\zeta_2\omega_{n2}-\tau)}{t_\varepsilon\omega_d\omega_{n2}^3}[H_2(t)-H_2(t-t_\varepsilon)], \tag{33a}$$

$$H_1(t)=\{e^{-at}[(\omega_d^2-a^2)\sin\ \omega_dt-2a\omega_d\ \cos\ \omega_dt]+2a\omega_d\}u(t), \tag{33b}$$

$$\begin{aligned}H_2(t)=&\{e^{-at}[(\omega_d^2-a^2)\sin(\omega_dt-\phi)-2a\omega_d\ \cos(\omega_dt-\phi)]\\&+(\omega_d^2-a^2+a\omega_{n2}^2t)\sin\ \phi+\omega_d(2a-\omega_{n2}^2t)\cos\ \phi\}u(t).\end{aligned} \tag{33c}$$

For a bushing with only a single fluid passage (as in B1), $f_{\mathrm{Th}}(t)$ is simplified by applying $2\zeta_2\omega_{n2}=\tau$ to Eqs. (30) and (33), with the parameters of Table 2 for model II.

Three transient input profiles are compared in Fig. 6(c). Observe that $x(t)=A_x\tanh(\sigma t)$ provides the best approximation to the measured excitation, and its continuous nature is essential to computation studies. Nevertheless, the $\tanh(\sigma t)$ function poses more difficulty in analytical work, unlike an ideal step or ramp function. Fig. 6(d) shows typical $f_T(t)$ responses to three excitation profiles. The main difference between the three responses lies in the region from $t=0$ to t_ε. Since a smoothened step or ramp function takes a longer time to reach the step height, the oscillations in $f_T(t)$ are delayed compared with the ideal step response. Further, the peak value in an ideal step response is $f_T(0_+)=A_x(k_r+\gamma+c_r\delta(t))$. However, for a ramp function approximated input, the peak value occurs at t_ε and is approximated by

$$f_T(t_\varepsilon)\approx A_xk_r+\frac{A_x\gamma}{t_\varepsilon\omega_d\omega_{n2}^2}\{e^{-at_\varepsilon}[(\omega_d^2-a^2)\sin\ \omega_dt_\varepsilon-2a\omega_d\ \cos\ \omega_dt_\varepsilon]+2a\omega_d\}. \tag{34}$$

Closed form expressions for $f_T(t)$, $p_1(t)$ and $p_2(t)$ to sinusoidal and step excitations will be utilized to examine the experimental results in the subsequent sections.

5. Role of key parameters and some limiting cases

5.1. Effect of long and short passage parameters

The effect of effective damping (c_{ie}) and mass (m_{ie}) on the transmitted force given smoothened step excitation is examined in Fig. 7, where c_{ie} and m_{ie} are the nominal values of the long passage (model II) for B1 configuration. The value of m_{ie} (adjusted by changing l_i or A_i) has a significant influence on the oscillation peak amplitude and period $T_d=2\pi/\omega_d$. When m_{ie} is increased, both T_d and peak values increase as seen in Fig. 7(a). This is because an increase in m_{ie} reduces ω_{n2} and ζ_2 and causes the exponential decay rate to decrease, as observed from Table 2 and Eq. (30). Note that for an ideal step response, $f_T(0_+)=A_x(k_r+\gamma+c_r\delta(t))$, and thus the peak value is not affected by m_{ie}. However, for smoothened step excitation (since the peak of $f_T(t)$ does not occur at $t=0_+$), the overshoot value is reduced when m_{ie} is decreased due to the higher oscillation frequency and exponential decay rate. As shown in Fig. 7(b), an increase in c_{ie} reduces the oscillation amplitude significantly and increases the decay rate; also the oscillation period $T_d=2\pi/\omega_d$ is slightly increased due to a reduction in ω_d. When c_{ie} is significantly reduced, say to $0.1c_{\mathrm{ie}}$, the step response is closer to the one for an undamped second-order system. Conversely, the $f_T(t)$ response is similar to that of a first-order system when c_{ie} is increased to a certain level, say $10c_{\mathrm{ie}}$.

The effect of short fluid passage parameters (c_{se} and m_{se} of model II) is examined as well. As shown in Fig. 7(c), when m_{se} is increased from its nominal value, the step response of $f_T(t)$ changes from the response of an over-damped second-order system to that of an underdamped system, since both ω_{n2} and ζ_2 are lower. However, a reduction in m_{se} alone has a trivial effect on $f_T(t)$. This implies that the effect of m_{se} is negligible when $m_{\mathrm{se}}/c_{\mathrm{se}}\ll m_{\mathrm{ie}}/c_{\mathrm{ie}}$. Fig. 7(d) shows that the $f_T(t)$ response has more oscillations when c_{se} is reduced. Conversely, when c_{se} is increased, the decay rate of $f_T(t)$ reduces, and the system no longer behaves like a second-order system. The nominal ω_{n2} of the short fluid passage is much higher since $m_{\mathrm{se}}\ll m_{\mathrm{ie}}$.

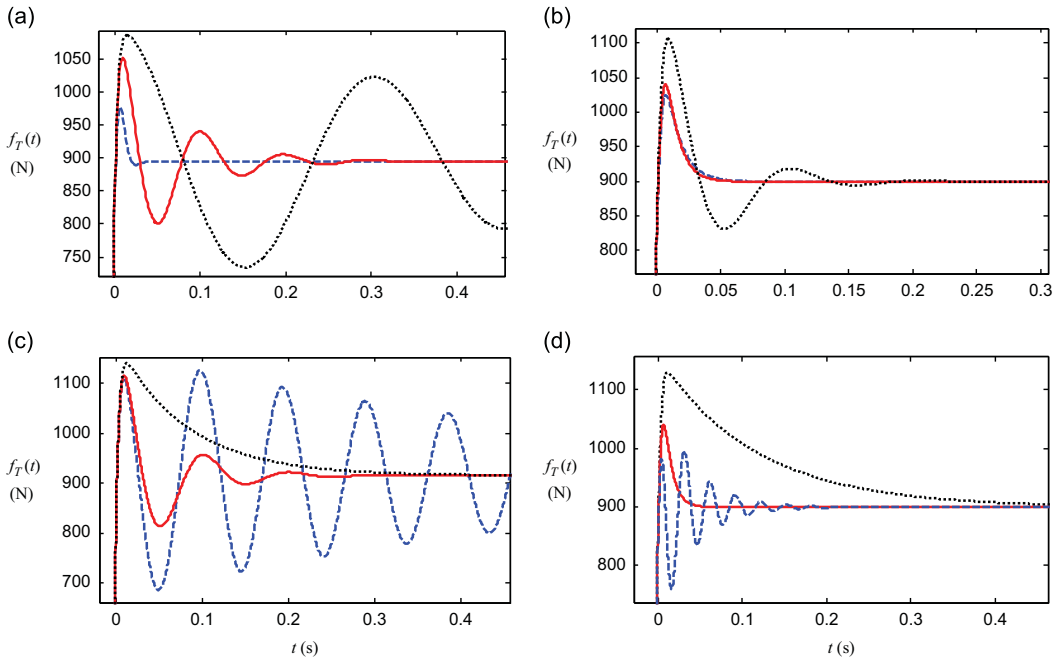

Fig. 7. Effect of long and short fluid passage parameters on the transient force time history given smoothened step excitation. (a) Effect of m_{ie}; (b) effect of c_{ie}; (c) effect of m_{se}; (d) effect of c_{se}. Key: ·····, $10m_{ie}$, $10c_{ie}$, $10m_{se}$ and $10c_{se}$; ——, $1.0m_{ie}$, $1.0c_{ie}$, $1.0m_{se}$ and $1.0c_{se}$; – – –, $0.1m_{ie}$ $0.1c_{ie}$, $0.1m_{se}$ and $0.1c_{se}$.

Table 3
Limiting cases of model II parameters.

Standard system parameters	Model II	$k_2=k_1$	$k_2 \ll k_1$	$k_2 \gg k_1$
γ	k_1+k_2	$2k_1$	k_1	k_2
ω_{n2}	$\sqrt{(k_1+k_2)/m_{ie}}$	$\sqrt{2k_1/m_{ie}}$	$\sqrt{k_1/m_{ie}}$	$\sqrt{k_2/m_{ie}}$
ζ_2	$\frac{c_{ie}}{2\sqrt{m_{ie}(k_1+k_2)}}$	$\frac{c_{ie}}{2\sqrt{2m_{ie}k_1}}$	$\frac{c_{ie}}{2\sqrt{m_{ie}k_1}}$	$\frac{c_{ie}}{2\sqrt{m_{ie}k_2}}$

Thus, the effect of c_{se} on the overshoot is more obvious than that of c_{ie}; this is confirmed by Fig. 7(d), where the overshoot value is reduced as c_{se} decreases.

5.2. *Effect of fluid chamber stiffness*

The effect of fluid chamber compliance is investigated by varying the stiffness ratio k_2/k_1 in model II. For the sake of illustration, define the nominal case as $k_1/k_2=1$, fix k_1 at its nominal value, and then vary k_2 from $100k_1$ to $0.1k_1$. The corresponding system parameters for the three limiting cases of $k_2/k_1 \gg 1$, $k_2/k_1 \approx 1$ and $k_2/k_1 \ll 1$ are listed in Table 3. When $k_2/k_1 \gg 1$, the amplitude of the transmitted force is significantly increased while its period is reduced, as shown in Fig. 8. This is because γ and ω_{n2} drastically increase as expected from Table 3 and Eq. (30). When k_2 is decreased from its nominal value, the oscillation period of $f_T(t)$ increases and its amplitude decreases. However, the oscillation decay rate is virtually unchanged since $\zeta_2\omega_{n2}=c_{ie}/(2m_{ie})$ is independent of k_1 or k_2. It is observed that the $f_T(t)$ response given smoothened step input is slightly affected when k_2/k_1 is decreased from 0.1 to 0.01; this is because now $\gamma \approx k_1$ and $\omega_{n2} \approx \sqrt{k_1/m_{ie}}$ when $k_2/k_1 \ll 1$. As mentioned in Sections 2, $k_2 \approx k_1$ for typical hydraulic bushings since the two chambers are usually similar. However, $k_2 \ll k_1$ is valid for hydraulic engine mounts since the lower chamber is usually bounded by a thin compliant rubber bellow. Thus this parametric study of the stiffness ratio provides a better understanding of the key difference between the hydraulic bushings and the hydraulic engine mounts.

6. Estimation of system parameters

The rubber path parameters (k_r and c_r) are estimated from a sinusoidal test of the drained bushing at very low frequencies where the hydraulic path does not contribute. Effective pumping areas A_1 and A_2 are approximated by $\Delta V/x_m$ where ΔV is the volume change under a static load f_m, and x_m is the mean displacement; also, it is assumed that $A_1 \approx A_2$. The chamber compliances C_1 and C_2 are estimated from rubber container elasticity, the liquid bulk modulus, and a contribution from the entrapped air. The fluid inertances are calculated as $I_i=\rho l_i/A_i$ and $I_s=\rho l_s/A_s$, where ρ is the fluid density, A_i and A_s are the cross-sectional areas, and l_i and l_s are the lengths of the long and short fluid passages, respectively. A flow bench test

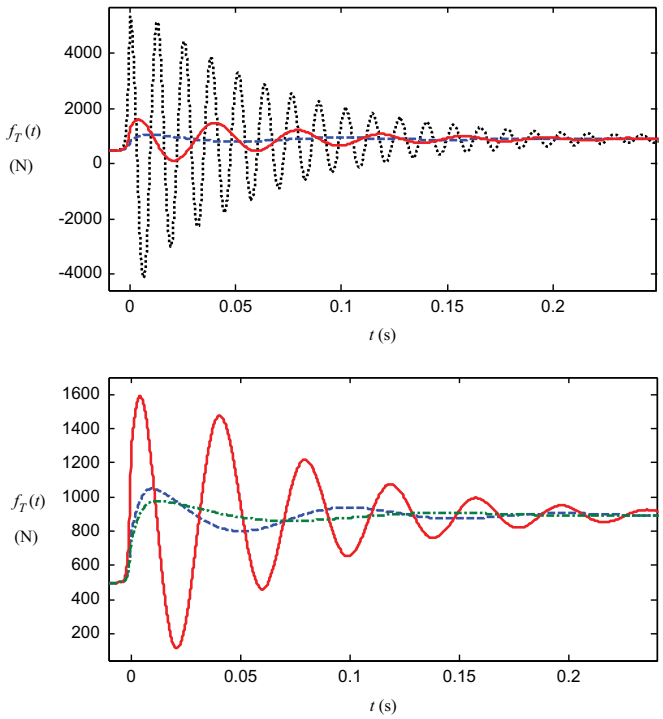

Fig. 8. Effect of hydraulic chamber stiffness on the transient force time history given smoothened step excitation. Key: ·····, $k_2=100k_1$; ——, $k_2=10k_1$; – – –, $k_2=k_1$; – · – ·, $k_2=0.1k_1$.

using water at room temperature yields q and Δp data for B1 and B2. By assuming the resistance (R) is linear in the operating regime (o), i.e. $\Delta p = Rq$, then R is calculated as $R = d\Delta p/dq\big|_o$. Then, equivalent mechanical system parameters are calculated. Furthermore, the configuration with all flow passages closed (B0) is tested to estimate k_1 and k_2 values; these are verified by the stiffness measurements of B0 at very low frequencies. Estimated parameters for sinusoidal responses are listed in Table 4.

Although most parameters estimated from the steady harmonic response such as the effective fluid mass, equivalent chamber stiffness, and rubber damping should be valid under transient excitations, the rubber stiffness and effective flow resistance of each flow passage must be re-estimated due to their sensitivity to the excitation amplitude and flow conditions. Consider the step responses of B1 and B3 as displayed in Fig. 9. With reference to Eqs. (26) and (27), observe that $f_T(t)$ converges to $A_x k_r$ as $t\to\infty$. Thus, k_r is estimated from this asymptotic value. The effective damping c_{ie} of the long flow passage is estimated from Eq. (30), which shows that $T_d = 2\pi/\omega_d$ and the envelope curve $\Xi(t) = A_x(\gamma e^{-\zeta_2\omega_{n2}t} + k_r)$ depend on c_{ie}. Likewise, c_{se} of the short fluid passage is estimated from the step response of B2. Regarding the response of the B3 configuration, Eq. (14) of model II is simplified by assuming that the inertia of an ideal orifice can be neglected at the lower frequencies; the expression is as follows where $\gamma = k_1 + k_2$ and $\tau_2 = (k_1 + k_2)/c_{oe}$ as defined in Table 2:

$$K_d(s) = K_{dr}(s) + K_{dh}(s) \approx (k_r + c_r s) + \left(\gamma \frac{s}{s+\tau_2}\right), \tag{35}$$

note that $K_{dh}(s)$ is now given by a first-order system expression. Thus the step response of B3 is approximated as

$$f_T(t) \approx A_x[k_r \tanh(\sigma t) + c_r \sigma \operatorname{sech}^2(\sigma t) + \gamma e^{-\tau_2 t}], \tag{36}$$

since k_1 and k_2 are obtained from the steady-state response of B0, c_{se} can be estimated from τ_2 in the step responses of B3. Parameter estimated for step responses are shown in Table 4 as well.

7. Analysis of measured harmonic responses in time domain

The measured time histories of $f_T(t)$ and $\Delta p(t) = p_2(t) - p_1(t)$ at several excitation frequencies and amplitudes are examined using the linear system theory as discussed above for each configuration. For instance, the transmitted force and pressure differential estimated by model II are compared in Fig. 10(a) and (b) with B1 measurements under 0.1 mm (p–p) excitation at 10 and 30 Hz. Excellent agreement is observed for $f_T(t)$, with an error in the peak to peak value of $f_T(t)$ around 3 percent at 10 Hz and 5 percent at 30 Hz. The predicted pressure amplitude at 10 Hz is slightly overestimated, with an error in $\Delta p(t)$ being about 15 percent at 10 Hz and 9 percent at 30 Hz; this may be caused by a minor underestimation of the effective damping at that frequency. Next the measured signals of B1 are transformed to the frequency domain by using a Fast Fourier Transform (FFT) algorithm. Only the fundamental frequency component is significant; the Fourier magnitudes at the second and third harmonics are usually 30 to 50 dB lower than the first one. This implies that the time history of $f_T(t)$

Table 4
Estimated model parameters for steady state harmonic and step responses.

Parameter	Sinusoidal response (X=0.1 mm)	Step-up response (A_e=A_x)	Step-down response (A_e=2A_x)
k_r (N/m)	5.3×10^5	4.0×10^5	4.2×10^5
c_r (N s/m)	200	200	200
k_1 (N/m)	1.1×10^5	1.1×10^5	1.1×10^5
k_2 (N/m)	1.4×10^5	1.4×10^5	1.4×10^5
m_{ie} (kg)	59.9	59.9	59.9
m_{se} (kg)	5.9	5.9	5.9
c_{ie} (N s/m)	1.2×10^3	2.2×10^3	3.6×10^3
c_{se} (N s/m)	1.5×10^3	3.0×10^3	4.6×10^3
c_{oe} (N s/m)	9.7×10^3	4.2×10^4	5.4×10^4

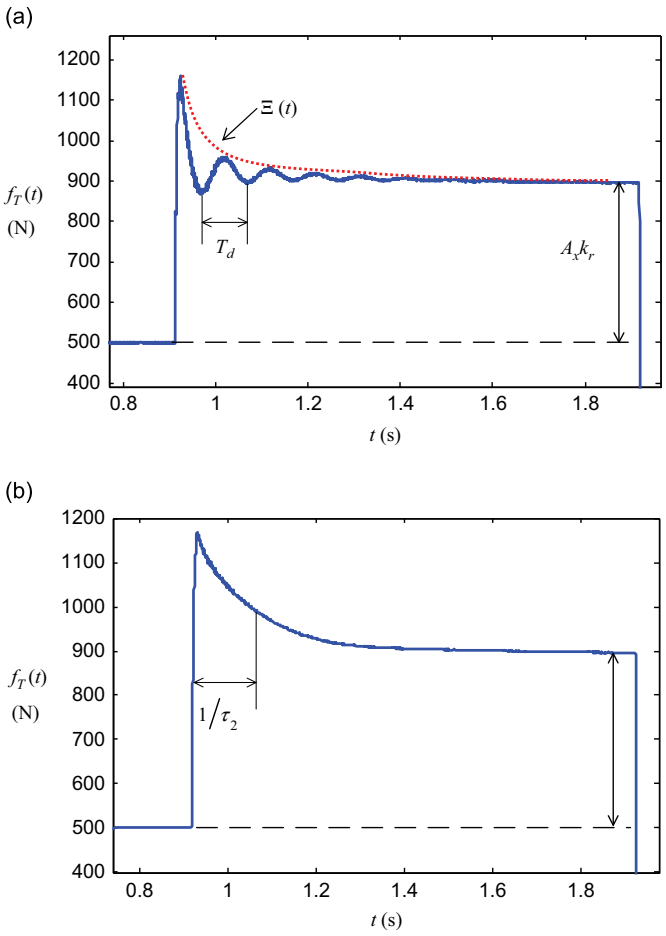

Fig. 9. Typical step-up force responses. (a) Step-up response of B1; (b) step-up response of B3. Key: ——, measured step-up response; ·····, envelope curve $\Xi(t)$.

can be approximated by a single harmonic term, and the sinusoidal response with one long flow passage is well represented by the proposed linear model.

8. Analysis of transient measurements under smoothened step excitations

To compare the three step-like responses, the response $f_T(t)$ are normalized by the step height A_e and then superposed in the same plot. The normalized step responses are categorized into three regimes as shown in Fig. 11. Regime 1 focuses on the overshoot, which is mainly controlled by the rubber path and chamber compliance such as k_r, c_r, k_1 and k_2. In fact, Eqs. (29) and (30) suggest that when $t_\varepsilon\to0$, i.e. when the smoothened step excitation takes negligible time to reach A_e, $f_T(0_+)\approx A_x(k_r+c_r\sigma+\gamma)$. Regime 2, where oscillations and the exponential decay of the step responses are seen, is dominated by the hydraulic path. Finally, regime 3 exhibits the asymptotic value, which is affected mostly by k_r as discussed in Section 6. Comparison of the three regimes shows that the two step-up responses (with A_e=A_x) have almost identical oscillatory and

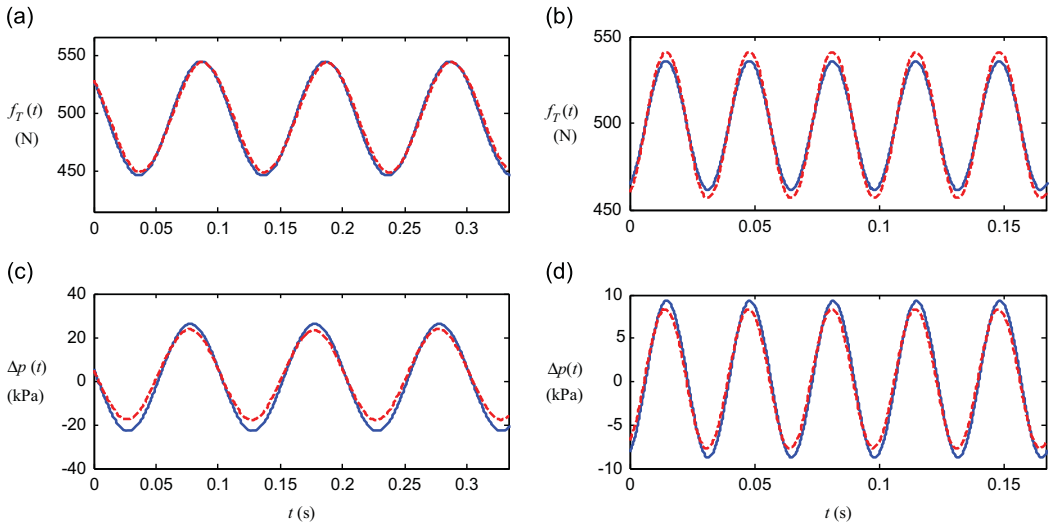

Fig. 10. Steady state sinusoidal responses of B1 with $X=0.1$ mm at 10 and 30 Hz. (a) Responses at 10 Hz; (b) responses at 30 Hz. Key: — — —, measured responses; ——, predictions of model II.

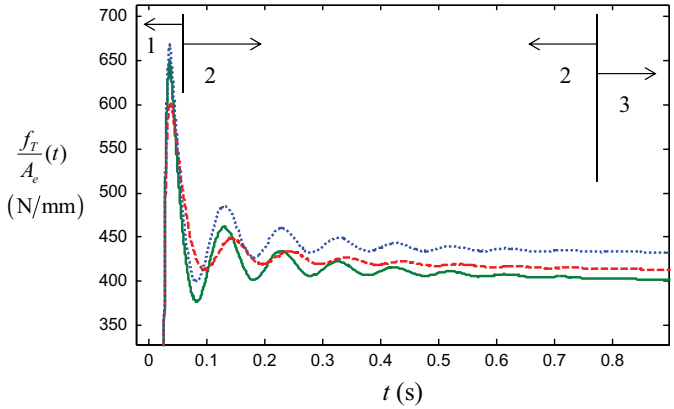

Fig. 11. Normalized step responses for B1 configuration. Here regime 1 focuses on the overshoot, regime 2 on the oscillation and exponential decay, and regime 3 on the asymptotic value. Key: ——, first step-up response with $A_e=A_x$; — — —, step-down response with $A_e=2A_x$; ·····, second step-up response with $A_e=A_x$; — · — ·, regimes.

decay responses. A difference between the asymptotic values may be due to the preload (f_m) dependence of rubber path properties (k_r and c_r). Further, the normalized step-down response (with $A_e=2A_x$) has a lower oscillatory peak value and a longer period than during the step-up event (with $A_e=A_x$). This implies changes in natural frequency and damping ratio when A_e is increased, which further suggests that the fluid resistance (effective damping c_{ie}) of a long flow passage depends on the step amplitude (A_e).

To examine the experimental results from the perspective of the analytical models developed in Section 4, first define the nominal values (subscript n) of the fluid resistance R_{i-n} as estimated from the steady flow test. Likewise, define the corresponding terms such as the nominal effective damping c_{ie-n} for the long flow passage. The predictions of model II with three effective damping values $c_{ie}=1.0c_{ie-n}$, $1.8c_{ie-n}$, $3.0c_{ie-n}$ are compared in Fig. 12 with the measured step-up and step-down responses of B1, and the key system parameters for the three different c_{ie} values are compared in Table 5. Observe that c_{ie-n} underestimates the damping in step responses, while $1.8c_{ie-n}$ gives a good approximation of step-up response trends with $A_e=A_x$; similarly, $3.0c_{ie-n}$ works for the step-down response with $A_e=2A_x$. This suggests that the effective damping increases when higher step amplitude (A_e) induces more flow, especially during the first two oscillation periods. Moreover, the measured $f_T(t)$ in the second half of regime 2 (in the response with $A_e=2A_x$ in Fig. 12(b)) has a better agreement with the prediction with $c_{ie}=1.8c_{ie-n}$, though $c_{ie}=3.0c_{ie-n}$ seems to work well in the first half of regime 2. This phenomenon is also observed in the step-up response with $A_e=A_x$. Further, the envelope curve $\Xi(t)$ of the step response of B1 does not follow the exponential decay of a linear system, and its oscillation period slightly decreases as $f_T(t)$ reaches an asymptotic value. These results again suggest that the fluid resistance R may be a function of flow rate, and the bushing system is indeed a nonlinear device.

The step responses of the configurations with two flow passages in parallel (B4 and B5) or in series (B6 and B7) are predicted by models I and III with parameters estimated from the single flow passage configurations (B1, B2 and B3). For instance, the step-up predictions (with $A_e=A_x$) of B5 with a long passage and orifice-like element in parallel are compared

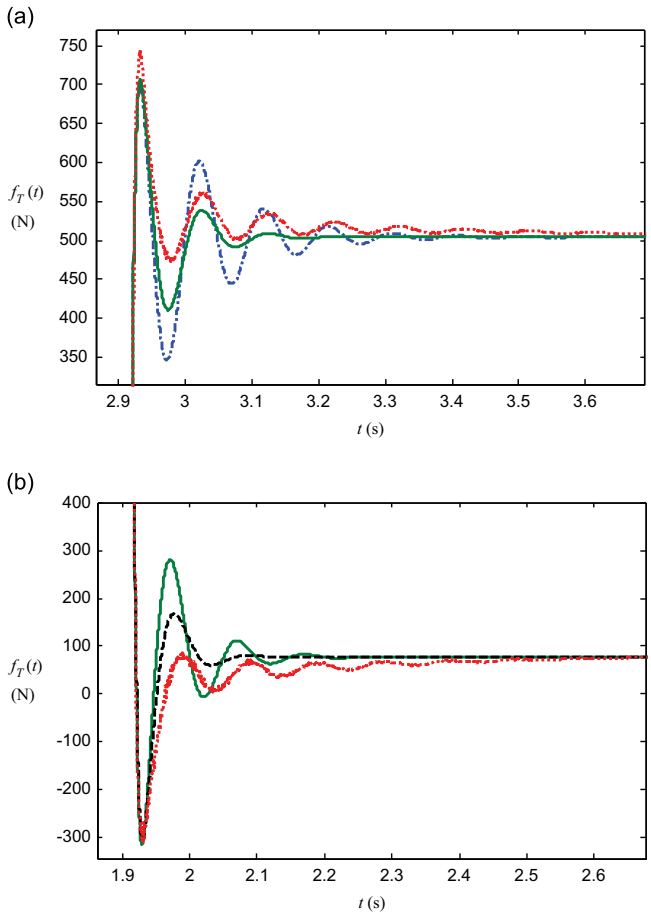

Fig. 12. Comparison of step responses for B1 with alternate fluid resistance values. (a) Step-up response with $A_e = A_x$; (b) step-down response with $A_e = 2A_x$. Key: ·····, measured response; – · – , prediction of model II with $c_{ie} = 1.0c_{i-n}$; ——, prediction of model II with $c_{ie} = 1.8c_{i-n}$; – – –, prediction of model II with $c_{ie} = 3.0c_{i-n}$.

Table 5
System parameters given three effective damping values for B1 configuration.

Effective damping c_{ie}	c_{ie-n}	$1.8c_{ie-n}$	$3.0c_{ie-n}$
System parameters	ω_{n2}	ω_{n2}	ω_{n2}
	ω_d	$0.97\omega_d$	$0.90\omega_d$
	ζ_2	$1.80\zeta_2$	$3.00\zeta_2$

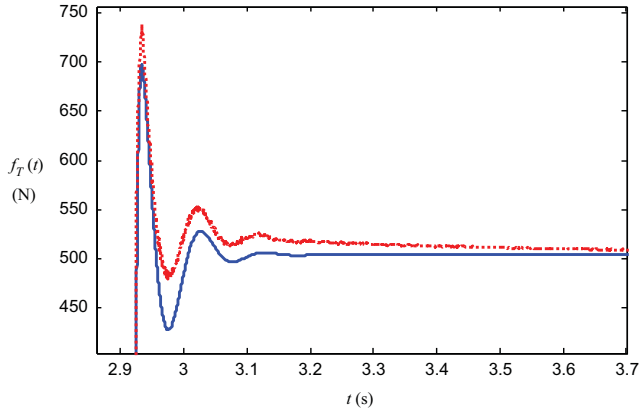

Fig. 13. Comparison of step responses for B5 configurations with $A_e = A_x$. Key: ——, prediction of model I; ·····, measured response.

with measurements in Fig. 13. Since c_{oe} is much higher than c_{ie}, the response is first dominated by the inertia track effect when the step excitation takes place. As the pressure differential between the two chambers decreases, the orifice-like element begins to allow more flow, and now increased damping decays the oscillations. In general, the B5 configuration has a higher effective damping than B1 but lower than the B2 configuration. Like the results of B1, the offset of the predicted and measured $f_T(t)$ is higher than the discrepancies in terms of the oscillatory peak to peak values, which implies that another exponential decay term may exist in the rubber path though it is not represented by the Kelvin–Voigt model.

9. Conclusion

The main contribution of this article is a comprehensive study of time domain responses of fluid-filled bushings since no prior publication has addressed this issue. By utilizing a newly designed laboratory device, typical fluid-filled bushing design features are scientifically examined; these include harmonic and transient responses of different combinations of long and short fluid passages and orifice-like elements. Seven specific configurations are designed and experimentally evaluated in terms of the dynamic measurements of transmitted force and internal pressures. By applying the linear system theory to lumped models, dynamic stiffness and pressure transfer functions for several typical hydraulic bushings are derived. Also, closed form time domain solutions under step excitation are obtained by the convolution method. Model parameters for steady state harmonic and transient responses are then successfully estimated, and experimental results are analyzed by using the linear model predictions. It is observed that the harmonic responses of most configurations (especially the one with a long inertia track), are well represented by the linear model under low amplitude excitations. Moreover, the proposed models are employed to detect system nonlinearities in the transient responses. It is observed from the measured and predicted step-up and step-down responses that the effective damping is highly dependent on the step amplitude and the fluid resistance significantly changes (during the transient event) in the subsequent cycles, which causes the system frequency and damping components to vary with time. This study also suggests that a reduction in the stiffness of rubber and fluid chambers could decrease the peak forces in the transient responses. Further, the effective damping of the fluid passage could be increased by reducing the diameter of the inertia track, by increasing its length or by adding a new flow restriction element. Finally, the proposed linear models provide a reasonable description of many practical bushing designs [1,2,6–11]. Nevertheless, future work should focus on the development of nonlinear models of hydraulic paths and improved visco-elastic characterization of the rubber path in order to predict their amplitude sensitivity and frequency-dependent properties.

Acknowledgment

We acknowledge the member organizations such as Transportation Research Center Inc., Honda R&D Americas, Inc., and YUSA Corporation of the Smart Vehicle Concepts Center (www.SmartVehicleCenter.org) and the National Science Foundation Industry/University Cooperative Research Centers program (www.nsf.gov/eng/iip/iucrc) for supporting this work. We also thank C. Gagliano and P.C. Detty for their help with the experimental studies.

Appendix A. Dynamic pressure expressions

To estimate the dynamic pressures inside the fluid chambers, the following transfer functions of model I are simplified as follows by assuming $A_1 \approx A_2$, where τ, ω_{n2}, and ζ_2 are the same as in Eq. (10):

$$G_1(s) = \frac{P_1}{X}(s) \approx -\frac{k_1}{A_1}\frac{s^2+\tau s}{s^2+2\zeta_2\omega_{n2}s+\omega_{n2}^2}, \quad G_2(s) = \frac{P_2}{X}(s) \approx \frac{k_2}{A_2}\frac{s^2+\tau s}{s^2+2\zeta_2\omega_{n2}s+\omega_{n2}^2}, \tag{A1a,b}$$

then the harmonic pressure time histories of $p_1(t)$ and $p_2(t)$ of a bushing with an inertia track and orifice-like element in parallel (as in B5) are obtained as follows from $x(t) \otimes g_1(t)$ and $x(t) \otimes g_2(t)$, where $g_1(t)$ and $g_2(t)$ are the impulse response of G_1 and G_2, respectively:

$$p_1(t) = -\frac{Ak_1}{A_1}\left\{\sin\,\omega t - \frac{\omega_{n2}}{2\sqrt{1-\zeta_2^2}}\left[\frac{E_1(t)}{\Gamma_1}+\frac{E_2(t)}{\Gamma_2}\right] + \frac{(2\zeta_2\omega_{n2}-\tau)}{2\sqrt{1-\zeta_2^2}}\left[\frac{E_3(t)}{\Gamma_1}+\frac{E_4(t)}{\Gamma_2}\right]\right\}, \tag{A2a}$$

$$p_2(t) = \frac{Ak_2}{A_2}\left\{\sin\,\omega t - \frac{\omega_{n2}}{2\sqrt{1-\zeta_2^2}}\left[\frac{E_1(t)}{\Gamma_1}+\frac{E_2(t)}{\Gamma_2}\right] + \frac{(2\zeta_2\omega_{n2}-\tau)}{2\sqrt{1-\zeta_2^2}}\left[\frac{E_3(t)}{\Gamma_1}+\frac{E_4(t)}{\Gamma_2}\right]\right\}, \tag{A2b}$$

where Γ_1, Γ_2, a, b, c, ω_d, $E_1(t)$ and $E_2(t)$ are defined in Eq. (25a)–(25j).

Similarly, by using the convolution method, the transient pressure responses of model I to an ideal step excitation are obtained as:

$$p_1(t) \approx -\frac{A_x k_1}{A_1 \omega_d} e^{-at}(a\ \sin\ \omega_d t + \omega_d\ \cos\ \omega_d t) + \frac{A_x k_1 (2\zeta_2 \omega_{n2} - \tau)}{A_1 \omega_{n2} \omega_d}\left\{e^{-at}[a\ \sin(\omega_d t - \phi) + \omega_d\ \cos(\omega_d t - \phi)] + a\ \sin\ \phi - \omega_d\ \cos\ \phi\right\}, \tag{A3a}$$

$$p_2(t) \approx \frac{A_x k_2}{A_2 \omega_d} e^{-at}(a\ \sin\ \omega_d t + \omega_d\ \cos\ \omega_d t) - \frac{A_x k_2 (2\zeta_2 \omega_{n2} - \tau)}{A_2 \omega_{n2} \omega_d}\left\{e^{-at}[a\ \sin(\omega_d t - \phi) + \omega_d\ \cos(\omega_d t - \phi)] + a\ \sin\ \phi - \omega_d\ \cos\ \phi\right\}. \tag{A3b}$$

When the smoothened step-up excitation is approximated by the hyperbolic–tangent function, the pressures inside two fluid chambers are derived as follows for model I, where the parameters are defined as in Eq. (30):

$$p_1(t) = -\frac{A_x k_1}{A_1}\ \tanh(\sigma t) + \frac{A_x k_1}{A_1} - \frac{A_x k_1}{A_1 \omega_d}\left\{e^{-at}[a\ \sin\ \omega_d t + \omega_d\ \cos\ \omega_d t] + 2\omega_{n2}^2 \Delta_1(t)\right\} + \frac{A_x k_1 (2\zeta_2 \omega_{n2} - \tau_1)}{A_1 \omega_{n2} \omega_d}\left\{e^{-at}[a\ \sin(\omega_d t - \phi) + \omega_d\ \cos(\omega_d t - \phi)] + a\ \sin\ \phi - \omega_d\ \cos\ \phi + 2\omega_{n2}^2 \Delta_2(t)\right\}, \tag{A4a}$$

$$p_2(t) = \frac{A_x k_2}{A_2}\ \tanh(\sigma t) - \frac{A_x k_2}{A_2} + \frac{A_x k_2}{A_2 \omega_d}\left\{e^{-at}[a\ \sin\ \omega_d t + \omega_d\ \cos\ \omega_d t] - \omega_d + 2\omega_{n2}^2 \Delta_1(t)\right\} - \frac{A_x k_2 (2\zeta_2 \omega_{n2} - \tau_1)}{A_2 \omega_{n2} \omega_d}\left\{e^{-at}[a\ \sin(\omega_d t - \phi) + \omega_d\ \cos(\omega_d t - \phi)] + a\ \sin\ \phi - \omega_d\ \cos\ \phi + 2\omega_{n2}^2 \Delta_2(t)\right\}. \tag{A4b}$$

For the ramp function approximated transient excitation, the pressures within the two fluid chambers are derived as

$$p_1(t) = -\frac{A_x A_1}{t_\varepsilon \omega_d \omega_{n2}^2 k_1}[H_1(t) - H_1(t - t_\varepsilon)] + \frac{A_x A_1 (2\zeta_2 \omega_{n2} - \tau)}{t_\varepsilon \omega_d \omega_{n2}^3 k_1}[H_2(t) - H_2(t - t_\varepsilon)], \tag{A5a}$$

$$p_2(t) = \frac{A_x A_2}{t_\varepsilon \omega_d \omega_{n2}^2 k_2}[H_1(t) - H_1(t - t_\varepsilon)] - \frac{A_x A_2 (2\zeta_2 \omega_{n2} - \tau)}{t_\varepsilon \omega_d \omega_{n2}^3 k_2}[H_2(t) - H_2(t - t_\varepsilon)]. \tag{A5b}$$

For a bushing with inertia track only (as in B1), pressures $p_1(t)$ and $p_2(t)$ are simplified by setting $2\zeta_2 \omega_{n2} - \tau = 0$ in the above equations, with system parameters of model II as listed in Table 2.

References

[1] W. Sauer, Y. Guy, Hydro bushings – innovative NVH solutions in chassis technology, SAE Paper 2003-01-1475, 2003.
[2] B. Piquet, C. Maas, F. Capou, Next generation of suspension bushings: reviews of current technologies and expansion upon new 3rd generation product data, SAE Paper 2007-01-0850, 2007.
[3] R.A. Ibrahim, Recent advances in nonlinear passive vibration isolators, *Journal of Sound and Vibration* 314 (2008) 371–452.
[4] N. Gil-Negrete, J. Vinolas, L. Kari, A nonlinear rubber material model combining fractional order viscoelasticity and amplitude dependent effects, *Journal of Applied Mechanics* 76 (1) (2009) 011009.
[5] N. Gil-Negrete, A. Rivas, J. Vinolas, Predicting the dynamics behaviour of hydro bushings, *Shock and Vibration* 12 (2005) 91–107.
[6] G.L. Hipsher, High damping resilient bushing, U.S. Patent No. 3642268, 1972.
[7] K. Konishi, Fluid-filled resilient bushing, U.S. Patent No. 4588174, 1986.
[8] R. Kanda, Fluid-filled resilient bushing with circumferential orifice, U.S. Patent No. 4693456, 1987.
[9] R. Kanda, Fluid-filled cylindrical elastic connector having two orifice passages with different cross sectional areas, U.S. Patent No. 5060918, 1991.
[10] S. Veverka, S. Roth, Hydraulic damping bushing, U.S. Patent No. 5040774, 1991.
[11] S.F. Roth, H.H. Henry III, Fluid-filled elastomeric suspension bushing, U.S. Patent No. 5397112, 1995.
[12] M. Lu, J. Ari-Gur, Study of dynamic properties of automotive hydrobushing, *ASME Design Engineering Division Proceedings* 106 (2000) 135–140.
[13] M. Lu, J. Ari-Gur, Study of hydromount and hydrobushing with multiple inertia tracks, *JSAE Annual Congress Proceedings 68-02*, 2002, pp. 5–8.
[14] M. Sevensson, M. Hakansson, Hydrobushing Model for Multi-body Simulation, MS Thesis, Lund University, 2004.
[15] S. Arzanpour, M. Golnaraghi, A novel semi-active magnetorheological bushing design for variable displacement engines, *Jounal of Intelligent Material Systems and Structures* 19 (2008) 989–1003.
[16] T. Chai, J.T. Dreyer, R. Singh, Dynamic stiffness of hydraulic bushing with multiple internal configurations, SAE Paper 2013-01-1924, 2013.
[17] R. Singh, G. Kim, P.V. Ravindra, Linear analysis of an automotive hydro-mechanical mount with emphasis on decoupler characteristics, *Journal of Sound and Vibration* 158 (2) (1992) 219–243.
[18] J.Y. Yoon, R. Singh, Estimation of dynamic force transmitted by hydraulic mount using motion and/or pressure measurements and quasi-linear models, *Noise Control Engineering Journal* 58 (4) (2010) 403–419.
[19] M. Tiwari, H. Adiguna, R. Singh, Experimental characterization of a nonlinear hydraulic engine mount, *Noise Control Engineering Journal* 51 (1) (2003) 36–49.
[20] J.C. Dixon, *The Shock Absorber Handbook*, 2nd edition, John Wiley & Sons Ltd., Chichester, 2007.
[21] MTS Elastomer Test System Model 831.50 (1000 Hz), ⟨http://www.mts.com⟩, 2004.